Journal of Alloys and Compounds 481 (2009) 673–680

Contents lists available at ScienceDirect

Journal of Alloys and Compounds

journal homepage: www.elsevier.com/locate/jallcom

Characterization of MgH_2 formation by low-energy ball-milling of Mg and Mg + C (graphite) mixtures under H_2 atmosphere

V. Fuster[a,*], G. Urretavizcaya[a,b], F.J. Castro[a,b]

[a] Centro Atómico Bariloche (CNEA, CONICET), R8402AGP, S. C. de Bariloche, Río Negro, Argentina
[b] Instituto Balseiro (UNCuyo), R8402AGP, S. C. de Bariloche, Río Negro, Argentina

ARTICLE INFO

Article history:
Received 18 December 2008
Received in revised form 9 March 2009
Accepted 12 March 2009
Available online 21 March 2009

Keywords:
Metal hydrides
Mechanical alloying
Thermal analysis
Microstructure
Magnesium

ABSTRACT

In the present work the formation of nanocrystalline magnesium hydride by reactive mechanical alloying (RMA) of a mixture of magnesium and 10 wt.% graphite flakes is reported. The synthesis was done at room temperature under 5 bar of hydrogen using a low-energy milling device. Magnesium without graphite was also milled as a reference material. We determine phase evolution by X-ray diffraction (XRD), thermal dehydriding properties by differential scanning calorimetry (DSC) and morphological and microstructural characteristics by laser granulometry, BET surface analysis, optical microscopy and scanning electron microscopy (SEM), at different stages of the milling process.

The formation of MgH_2 occurs faster in the graphite added material, due to the lubricant properties of graphite. It reaches a hydrogen capacity of 6.2 ± 0.1 wt.% H in 50 h, whereas the reference material needs 100 h to load 7.1 ± 0.1 wt.% H. During the synthesis, both materials follow the same sequence of microstructural and morphological changes, though in different time scales. After the synthesis, both materials present similar microstructural and morphological characteristics. As regards dehydriding properties, we found that graphite plays a catalytic role in the decomposition of magnesium hydride. The graphite added material decomposes always at lower temperatures than the reference material. Additionally, we observe that particle size instead of crystallite size is the relevant property that influences hydrogen desorption kinetics.

1. Introduction

Metal hydrides are materials of considerable interest for safe and practical hydrogen storage. Magnesium-based systems are intensively investigated due to magnesium's high theoretical storage capacity (7.6 wt.%), light weight, and availability [1,2]. However, its low sorption kinetics below 200 °C and high operation temperatures do not meet the industry requirements for practical applications. To overcome these drawbacks, many efforts have been made. For example, focusing on the synthesis method, it has been shown that ball-milling is an effective technique for activating and improving the hydrogen sorption properties of magnesium by microstructural modification. The microstructure acquired by milling enhances gas–solid interaction and reduces diffusion paths. Moreover, reactive mechanical alloying (RMA) has been widely used as a technique to directly synthesize hydrides with very small particle size [3–10]. Another approach to improve Mg properties has been the incorporation of various additives with catalytic function, sometimes by mechanochemical treatments: (a) transition metals, such as Nb [11–13], Ti [12,14], V [14] and Fe [15,16] and/or their alloys; (b) mixed valence transition metal oxides, such as Cr_2O_3 [17,18], WO_3 [19], Nb_2O_5 [20,21]; (c) salts [22]; and (d) carbon allotropes, such as carbon nanotubes [23–27], carbon black [26,27], fullerenes [26] and graphite [9,24–39]. Focusing on the addition of graphite by mechanical milling, three main routes can be identified: (1) milling Mg and graphite under inert atmosphere [28–34,36,39], (2) milling MgH_2 and graphite under inert atmosphere [24,26,35,37,40], and (3) milling Mg and graphite under reactive H_2 atmosphere [9,23,25,27,38]. Irrespective of the incorporation route, there are some aspects upon which there is consensus in the literature and some others which remain controversial. For instance, everybody agrees that graphite improves the hydrogen sorption properties of magnesium [9,24–39]. Additionally, many authors have proved that graphite protects magnesium from oxidation [31,32,35,40], that graphite acts as a process control agent which improves the milling process thanks to its lubricant properties [24,25,27,31,32,35,38,40] and that the crystallite size is not relevant for sorption kinetics [26,31,32,37]. However, many aspects remain controversial. For example, some authors believe that graphite plays a catalytic role on hydrogen sorption [25–27,38],

* Corresponding author at: Centro Atómico Bariloche (CNEA), Av. Bustillo 9500, R8402AGP, S. C. de Bariloche, Río Negro, Argentina. Tel.: +54 2944 445197; fax: +54 2944 445190.
E-mail addresses: fusterv@cab.cnea.gov.ar, valfuster@gmail.com (V. Fuster).

0925-8388/$ – see front matter © 2009 Elsevier B.V. All rights reserved.
doi:10.1016/j.jallcom.2009.03.056

whereas a few others do not [24,35]. An ample majority agrees that the improvement in sorption kinetics is not due to the small particle size obtained by milling [25–27,31,32,38,40], but some people think the opposite [35]. Several authors claim that avoiding graphite amorphization induced by milling is important for improving sorption kinetics [28–34,39], instead others argue hat it is not relevant [25,27,38]. Finally, a number of scientists believe that graphite prevents particle and crystallite growth [24], yet others state to the contrary [40]. Summarizing, one can conclude that the effect of carbon on the properties of magnesium-based hydrogen storage materials is complex and yet not clear.

In this work we try to clarify some of these unresolved aspects by studying the formation of magnesium hydride during the reactive mechanical alloying (under hydrogen atmosphere) of magnesium with and without 10 wt.% of graphite. As we want to study in detail the hydride formation process, we choose as milling device a low-energy milling apparatus which allows us to "see" intermediate steps during the evolution of the milled materials. Such steps would pass unnoticed if we employed a high-energy mill, because of the short times typically involved in that case to obtain a material with similar characteristics.

2. Experimental

Magnesium powder (99%, Riedel de Haën) and a mixture of magnesium powder and 10 wt.% graphite flakes (99.9%, Sigma–Aldrich) were ball-milled under 5 bar of hydrogen (99.999%, Air Liquide). Both systems will be referred hereinafter as (Mg) and (Mg+10G), respectively. The milling was performed at room temperature using a low-energy milling device with a double magnet in the bottom vertical position (Uni-Ball-Mill II, Australian Scientific Instruments). The ball-to-powder mass ratio was 44:1 and the rotational speed was 196 rpm. A pressure transducer (PX181-100G5 V, Omega Engineering Inc.) and a portable memory (Hobo, Onset Computer Corp.) were attached to the milling chamber to acquire hydrogen pressure data. From these data, and using the ideal gas law, the hydrogen content in the sample was determined. The milling chamber was regularly purged and refilled with hydrogen to ensure a constant pressure. After each milling step, pressure data were acquired during 10 h to verify the absence of leaks. The milling was done until magnesium was fully hydrided. For (Mg) the milling took 100 h, whereas for (Mg+10G) it lasted 50 h.

At intermediate milling times as well as when achieved full completion of the hydride synthesis, samples were systematically extracted in an Ar-filled glove box (oxygen level below 3 ppm) to analyze the material evolution by X-ray diffraction (monochromated Cu Kα, PW1710/01, Philips Electronic Instruments), differential scanning calorimetry (DSC 2910, TA Instruments), laser granulometry in ethanol (Malvern Mastersizer hydro 2000S analyzer), BET surface area (Quantachrome Autosorb 1), optical microscopy (Leica DMRM) and scanning electron microscopy (SEM 515, Philips Electronic Instruments). For the optical microphotographs the powder was included in plastic resin (Prodyser PL-301 epoxy resin and EL-201/1 hardener) and polished with a 3:1 mixture of ethanol:glicerine. To avoid sample degradation by air exposure during the X-ray diffraction (XRD) measurements, the samples were prepared inside the glove box in a dedicated environmental chamber filled with Ar, later attached to the diffractometer. The materials crystallite size was estimated using the Scherrer equation [41]. The average of the integral breadth of the (1 0 0), (0 0 2), (1 0 1) peaks and of the (1 1 0), (2 1 1) peaks was used in the case of Mg and β-MgH_2, respectively. The DSC runs were done at a heating rate of 6 °C/min from room temperature up to 450 °C, and under an argon flow of 122 ml/min. The measurements were performed immediately after the extraction of each sample from the milling device, to avoid aging phenomena affecting the results. The hydrogen capacity was determined from the area under the curve and using a molar enthalpy equal to 76.1 kJ mol^{-1} [42].

3. Results and discussion

3.1. Synthesis of magnesium hydride

During milling, the H_2 pressure inside the milling chamber decreases due to MgH_2 formation. The hydriding curves obtained from this decrease are presented in Fig. 1. By milling the material without additive, a hydriding curve with a quasi-sigmoidal shape was obtained. Three distinct stages are identified: (1) an initial stage from 0 to 35 h, with an hydrogen uptake rate approximately constant and equal to 0.06 wt.% H per hour, (2) a second stage from 35 to 60 h, where the hydrogen uptake markedly augments to 0.15 wt.% H per hour, and (3) a final stage from 60 to 100 h where a progressively decreasing rate due to reactive exhaustion can be seen. After 100 h of milling, the material does not absorb hydrogen anymore and achieves a hydrogen capacity of 7.1 ± 0.1 wt.% H (93% of the theoretical capacity).

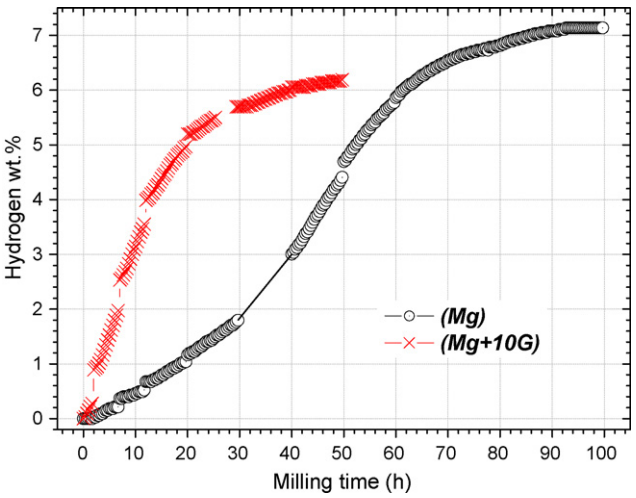

Fig. 1. Hydriding curves of (Mg) (⊙) and (Mg+10G) (×) during milling.

When (Mg+10G) is milled, we first notice that the total hydriding time practically halves. We also observe a few jumps in hydrogen content which correspond to pressure drops during the rest steps. A detailed analysis of these pressure drops is outside the scope of this manuscript and will be presented elsewhere. We only want to mention here that they are not caused by a leak, and are not the consequence of a decrease in gas temperature; their characteristic $t^{1/2}$ time dependence suggests that they correspond to hydrogen diffusion into Mg. The hydriding curve as a whole also involves three stages. Initially there is an incubation stage (not shown in the figure and not taken into account for time counting) that lasts approximately 12 h. During this period, where no hydrogen pressure drop is observed, milling mainly proceeds by low-energy shearing mode, probably due to the mechanical characteristics of the mixture, the size distribution of the powder and the lubricant properties of graphite. As milling proceeds, the above mentioned properties gradually evolve in such a way that the milling mode changes into a combination of high-energy shearing and impact [43]. During the second stage, from the end of the incubation period up to 15 h, hydrogen is absorbed at a constant rate equal to 0.28 wt.% H per hour, nearly twice the highest rate observed for (Mg). At the end of this stage, 70% of the hydride is already formed. The third and final stage, from 15 to 50 h, is similar to the final stage of (Mg), and corresponds to reaction completion. The hydriding degree after 50 h of milling is 6.2 ± 0.1 wt.% H (90% of the theoretical value). The higher hydriding rates observed for (Mg+10G) are mainly due to a more efficient milling process as a consequence of graphite addition. During milling graphite acts as a process control agent that due to its well-known lubricant properties reduces cold welding and, in this way, accelerates particle size reduction, which in turn improves hydriding rates. A similar behaviour has been reported previously [24,25,27,31,32,35,38,40].

3.2. X-ray analysis

Figs. 2 and 3 present the X-ray diffraction patterns of (Mg) and (Mg+10G), respectively, as a function of milling time. As regards (Mg), after 2 h of milling only the characteristic reflections of Mg are found, with a noticeable texture effect. According to the diffraction card JCPDS 35-0821, the (1 0 1) magnesium peak, located at

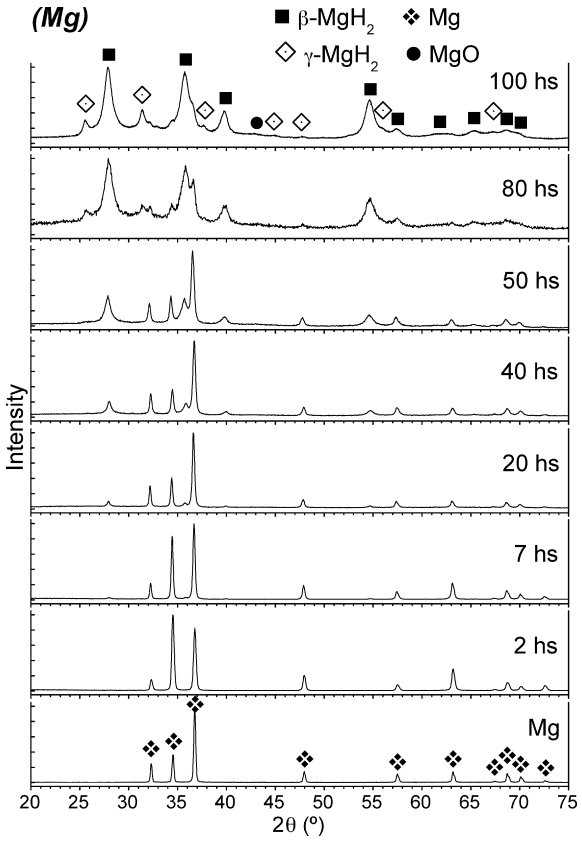

Fig. 2. X-ray diffraction patterns of (Mg) for different milling times. The pattern corresponding to the starting magnesium is also shown.

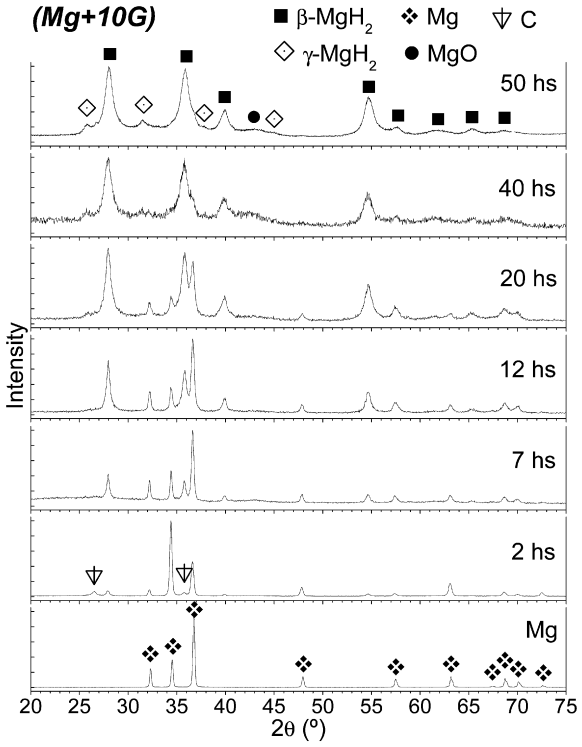

Fig. 3. X-ray diffraction patterns of (Mg+10G) for different milling times. The pattern corresponding to the starting magnesium is also shown.

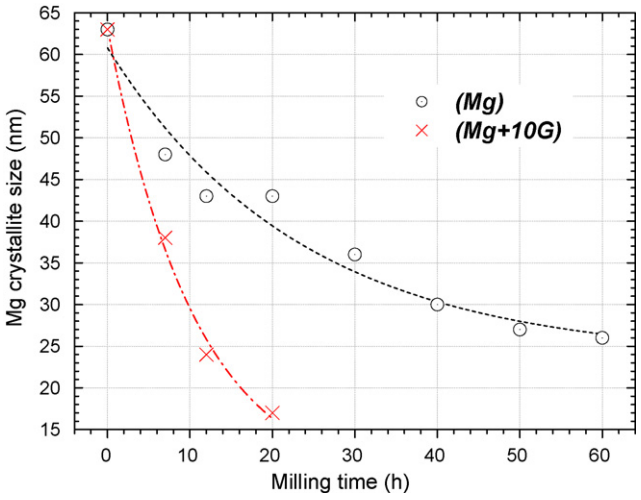

Fig. 4. Magnesium crystallite size of (Mg) (⊙) and (Mg+10G) (×) as a function of milling time. The starting material crystallite size (0 h) is also indicated. The lines are guides for the eye.

$2\theta = 36.8^\circ$, should have the maximum intensity. Our results indicate that the intensity of the (0 0 2) peak, located at $2\theta = 34.5^\circ$, is higher than that of the (1 0 1) peak, in agreement with previous reports [31]. This signifies that more crystallites corresponding to the basal plane of the hexagonal structure are exposed, which is consistent with the main slip system for hexagonal materials: the basal plane. Preferential orientation diminishes with further milling, and after 20 h disappears. As milling proceeds, the Mg diffraction peaks broaden due to the refinement of crystallite size and the accumulation of lattice strain and defects. Simultaneously, the intensity of these peaks weakens as Mg reacts with hydrogen. After 100 h, Mg main reflections cannot be distinguished. Typical X-ray reflections of the stable tetragonal β-MgH_2 (JCPDS 12-0697) are found after 7 h of milling. Additionally, the metastable orthorhombic γ-MgH_2 (JCPDS 35-1184) can be seen after 40 h of mechanical milling (H content equal to 3 wt.%). The formation of this phase is a consequence of the processing method by ball-milling [7,8]. The peak intensity of both hydrides increases as milling proceeds and peak width enlarges due to the same microstructural modifications induced by milling already described for Mg. At the last stages of milling, small reflections of MgO (JCPDS 45-0946) can be seen.

In the case of (Mg+10G) (Fig. 3), after only 2 h of milling the characteristic reflections of β-MgH_2 can be seen, together with peaks of graphite (JCPDS 41-1487) and magnesium. Mg also shows the aforementioned texture effect, which disappears after 7 h of milling. Additionally, no peak shift is found, in agreement with the Mg-C binary phase diagram that reports no solubility of C in Mg [44]. As milling proceeds Mg peaks weaken while the hydride typical reflections increase. Interestingly, the metastable γ-MgH_2 is formed after only 12 h of milling (H content equal to 4.0 wt.%), less than one-third of the time necessary when graphite is not present. Magnesium main peaks are indistinguishable after 50 h of milling.

In Fig. 4 the magnesium crystallite size as a function of milling time can be followed. The general trend, as usual for milled materials, is a decrease of crystallite size. In (Mg+10G) the decrease is more pronounced than in (Mg). This is a consequence of the more efficient milling process that takes place when graphite is added to Mg. The crystallite size goes from 63 nm in the starting powder to 26 nm after 60 h of milling for (Mg), and to 17 nm after only 20 h of milling for (Mg+10G).

In Fig. 5 the crystallite size of magnesium hydride as a function of milling time is presented. In both materials, when the typical X-ray reflections of the β-phase are clearly observed, the crystallites

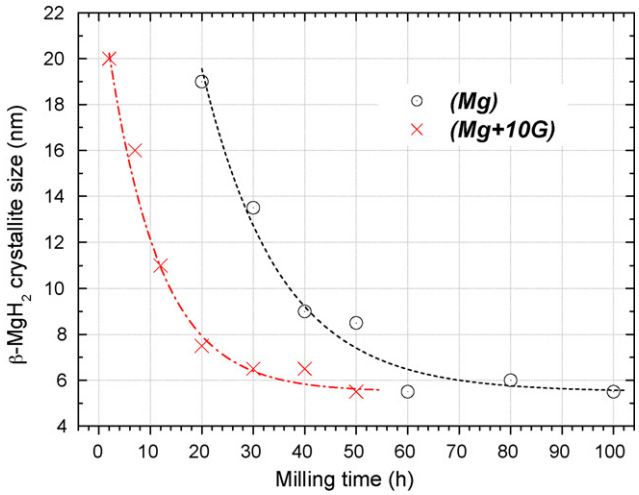

Fig. 5. Magnesium hydride crystallite size of (Mg) (⊙) and (Mg+10G) (×) as a function of milling time. The lines are guides for the eye.

have a mean size of 19 nm after 20 h of milling for (Mg) and 20 nm after 2 h of milling for (Mg+10G). The hydride grains are further refined by reactive mechanical milling down to the nanosize scale: approximately 6 nm after 100 h of milling for (Mg), and after 50 h of milling for (Mg+10G).

3.3. Thermal decomposition of magnesium hydride

Fig. 6 shows the DSC curves obtained after different milling times for (Mg). Only endothermic events are found, and they correspond to magnesium hydride decomposition. After 7 h of milling (Mg), a small peak at 400 °C associated to the thermal decomposition of β-MgH_2 can be seen. From this milling time up to 30 h, the area under the peak grows as a consequence of the increase in the amount

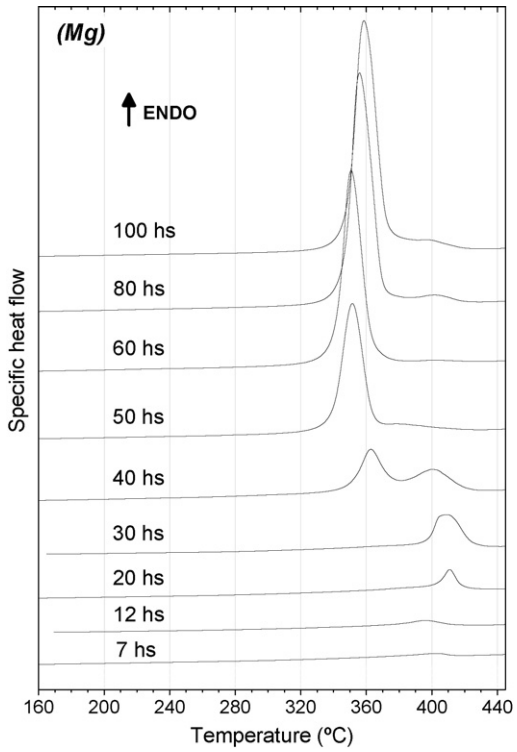

Fig. 6. Evolution of the DSC curves of (Mg) with milling time.

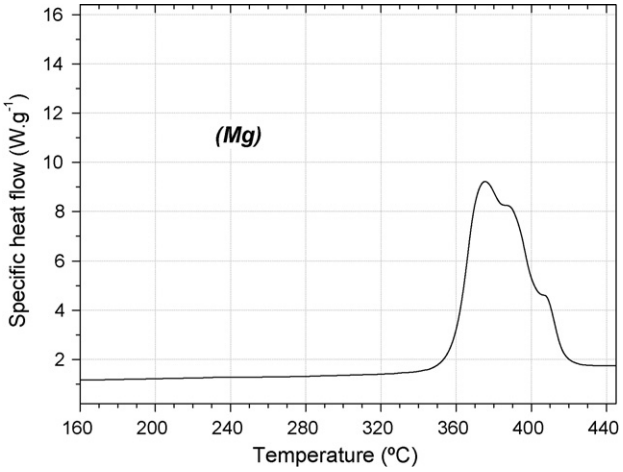

Fig. 7. DSC curve of (Mg) milled 100 h, dehydrided at 30 kPa and re-hydrided at 1000 kPa of H_2 and 325 °C in a Sievert-type apparatus.

of hydride (the evolution of the hydriding degree obtained from the peak area is closely analogous to the corresponding curves in Fig. 1 for both materials). After 40 h of milling, a noticeable splitting of the DSC curve can be seen. This splitting coincides with γ-MgH_2 formation (Fig. 2) and with the beginning of the second (faster) stage of milling (Fig. 1). It is also concurrent with the observation of smaller particles in the material (see below). From 50 h on, hydrogen desorption occurs mainly around 360 °C. Additionally, a very small hump near 400 °C can also be seen. The splitting of the DSC peak after 40 h of milling was interpreted as a synergetic effect induced by the metastable γ-MgH_2 [8]. Within this explanation, the low-temperature peak corresponds to the complete dehydriding of the γ-phase and the partial thermal decomposition of the β-phase, whereas the high-temperature peak corresponds to the dehydriding of the remaining β-MgH_2. However, Varin et al. [43] proposed a relationship between the particle size distribution in the powder and the decomposition temperature of MgH_2. The smaller the particle size, the lower the decomposition temperature. In order

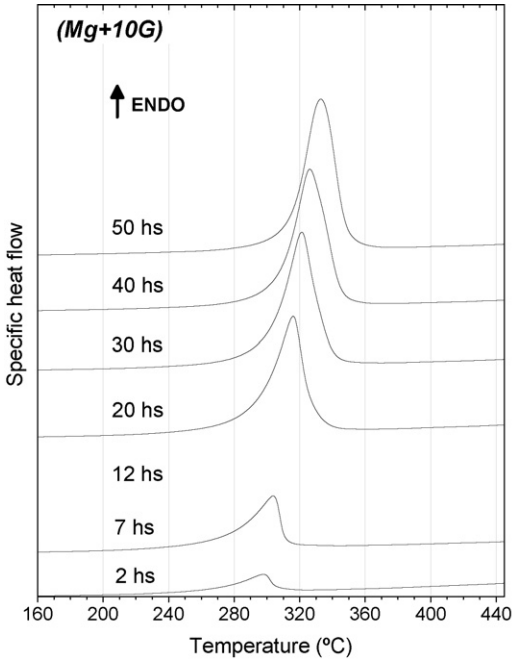

Fig. 8. Evolution of the DSC curves of (Mg+10G) with milling time.

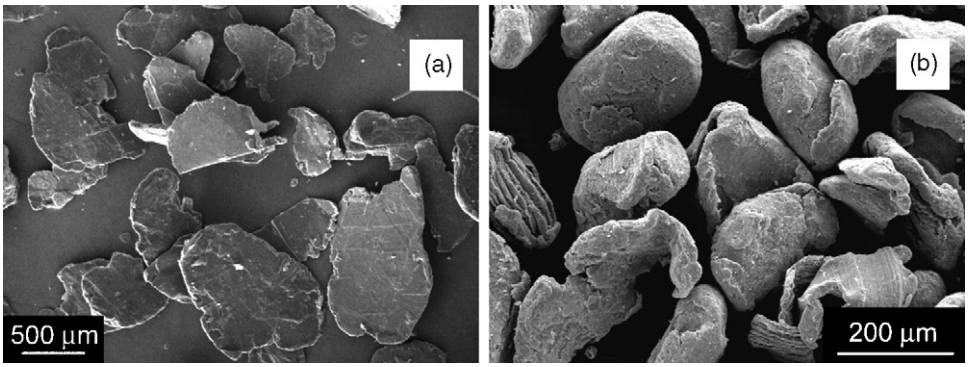

Fig. 9. SEM microphotograph of (a) graphite flakes and (b) as-received magnesium.

to clarify if the hydride temperature decomposition diminution is a consequence of γ-MgH_2 formation or particle size refinement, we made a DSC run of (Mg) milled 100 h after being dehydrided and re-hydrided in a volumetric apparatus at 325 °C under 30 and 1000 kPa, respectively (see Fig. 7). The XRD pattern of the re-hydrided material showed only the presence of β-MgH_2, with a crystallite size equal to 138 nm, according to Scherrer's equation. We see that irrespective of the γ-phase absence, the desorption of the re-hydrided material begins at low temperature. The corresponding peak is located at 375 °C, a temperature quite close to the peak temperature of the 100 h milled material, 360 °C, and far from the desorption temperature when no γ-MgH_2 is detected, 400 °C. This result suggests that the low-temperature decomposition of the hydride obtained after 100 h of milling is not only due to the presence of γ-MgH_2 but mainly to the small particle size obtained by mechanical milling, in agreement with [43,45]. However, this result does not discard a γ-MgH_2 effect in the 40 h milled material. Most likely both effects contribute to lower the desorption temperature. At the initial stages of milling, when particle size refinement is not much significant, the γ-MgH_2 effect could play the major role. Later on, when particle size has been reduced substantially, the particle size effect could prevail over the gamma effect. As an additional

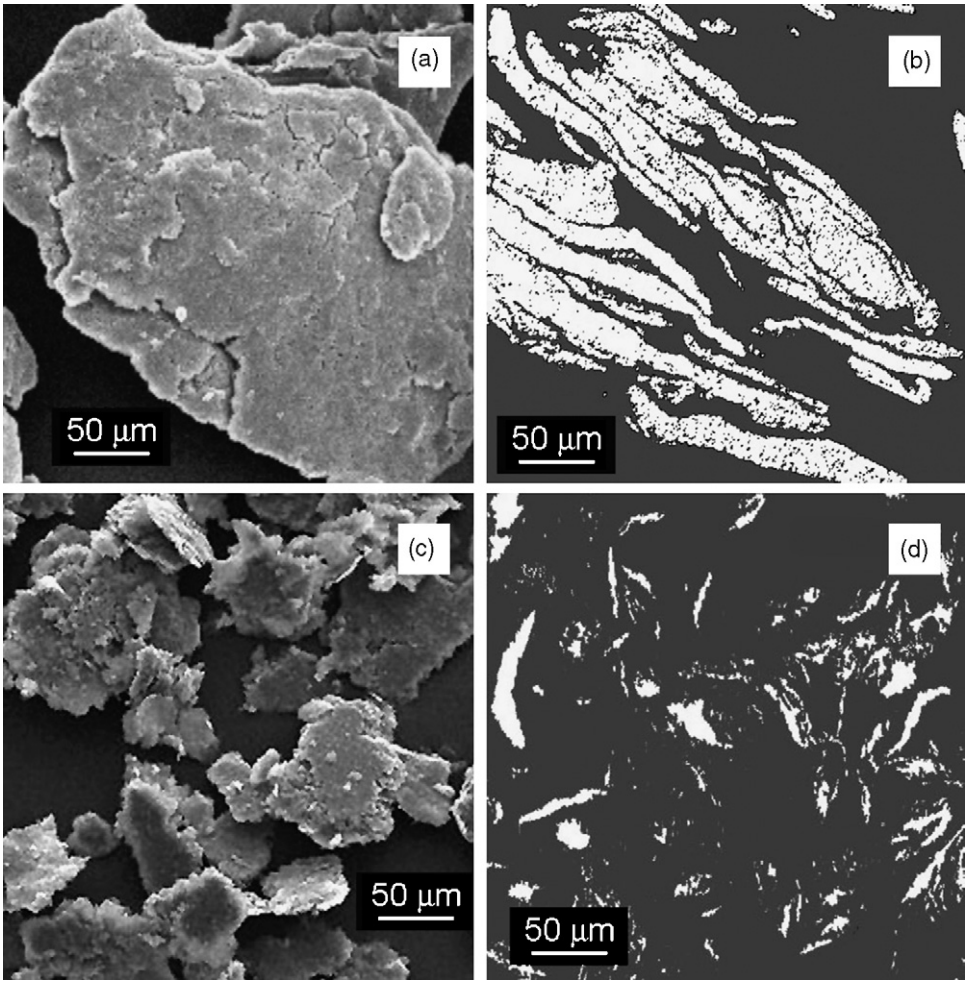

Fig. 10. Microphotographs of powders after 2 h of milling: (a) (Mg) SEM, (b) (Mg) optical (included), (c) (Mg+10G) SEM and (d) (Mg+10G) optical (included).

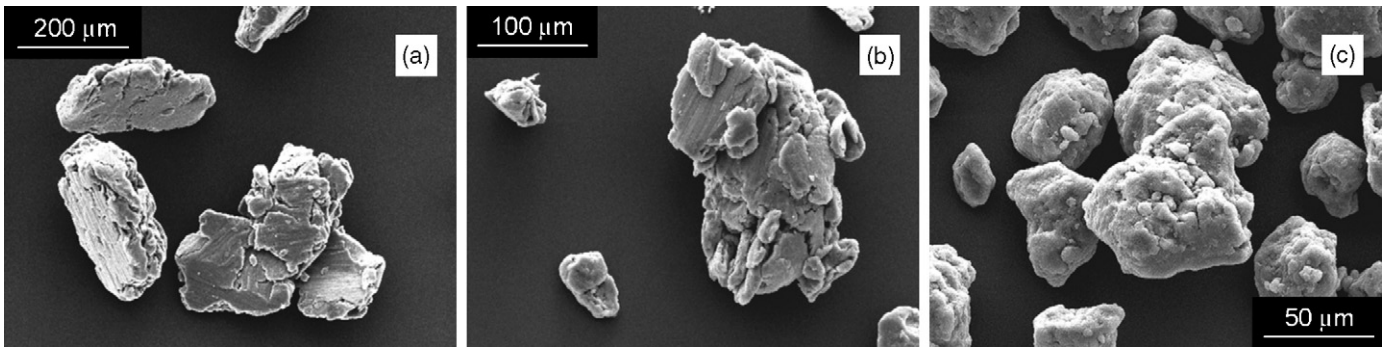

Fig. 11. SEM microphotographs of (Mg) powders after (a) 7 h, (b) 12 h and (c) 30 h of milling.

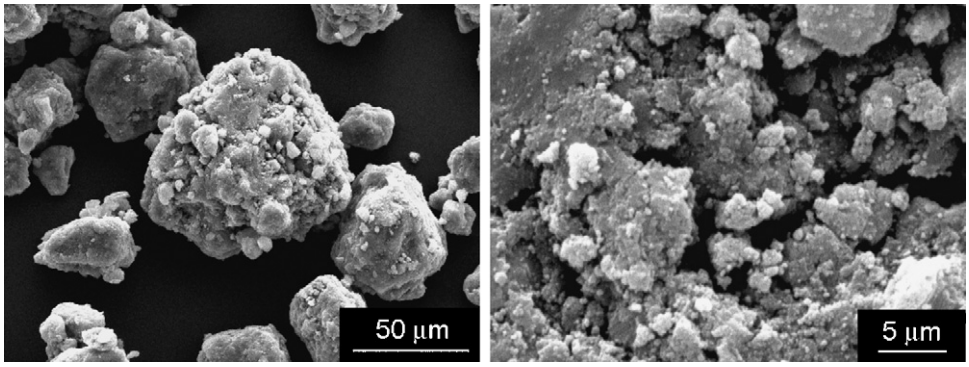

Fig. 12. SEM microphotographs of (Mg) after 40 h of milling.

comment, we see that the decomposition of the re-hydrided material occurs only 15 °C above that of the 100 h milled (Mg). Since the former has a hydride crystallite size more than 20 times larger than the grain size of the as-milled material, while the particle size is similar in both cases, then crystallite size is not the property that controls the improvement in hydrogen desorption kinetics in (Mg), which is consistent with previous reports [26,31,32,37,46,47].

Concerning (Mg+10G) (Fig. 8), the endothermic event associated with the thermal decomposition of β-MgH_2 can be observed after only 2 h of milling, with a peak centered at 300 °C, which is 60 °C below the lower decomposition temperature of (Mg). As milling proceeds, the peak area augments and its maximum temperature slightly shifts to higher values, reaching 330 °C after 50 h of milling. The fact that (Mg+10G) desorbs at 300 °C after only 2 h of milling suggests that graphite is acting as a catalyst for hydrogen desorption. In the case of (Mg), we have seen that two main processes contributed to lower the desorption temperature, namely particle size reduction and γ-MgH_2 presence. In this case, after only 2 h of milling there is no γ-MgH_2, and particle size reduction, as will be seen below, has just begun. Therefore, a graphite catalytic effect is the only cause that remains to explain the substantial lowering of the decomposition temperature.

In contrast to (Mg), no DSC doublets are observed in the decomposition of (Mg+10G) at any stage of milling. It seems that the graphite catalytic effect prevails over both the γ-phase and the particle size effects. Moreover, the slight shift of desorption temperature towards higher values in (Mg+10G) could be a consequence of the decrease of graphite concentration on the surface. As milling proceeds, the microstructure and particle size of (Mg+10G) evolves in a direction that should improve hydrogen desorption. Notwithstanding this, desorption moves towards higher temperatures. This could be explained as a consequence of the intermixing between graphite and magnesium, and the ensuing decrease of graphite concentration on the surface, where it may be playing its catalytic role. In turn, this points to a surface controlled desorption process, as has already been reported for similar systems [48].

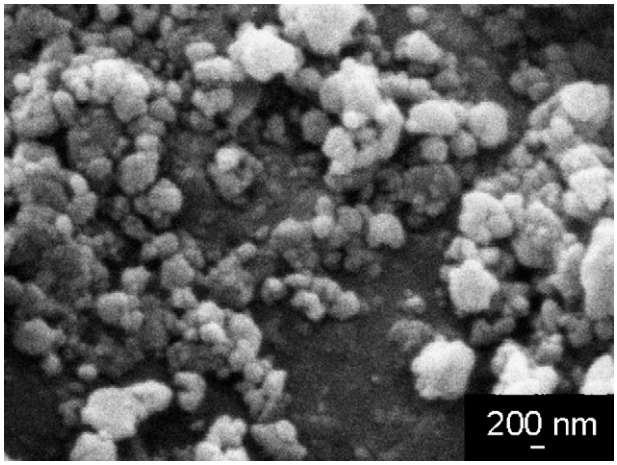

Fig. 13. SEM microphotograph of (Mg+10G) after 50 h of milling, showing in detail the surface of a typical agglomerate.

3.4. Morphological analysis of reactants and reactively milled powders

Figs. 9–13 present SEM and optical microphotographs of the studied materials. The optical photos correspond to powder included in epoxy resin and properly polished to reveal sections of particles and agglomerates.

The starting materials can be seen in Fig. 9. The graphite powder consists of flat, shiny and steel gray platelet-like particles (Fig. 9a). The typical structure of layers superposed and easily separable can be appreciated. The as-received magnesium powder is character-

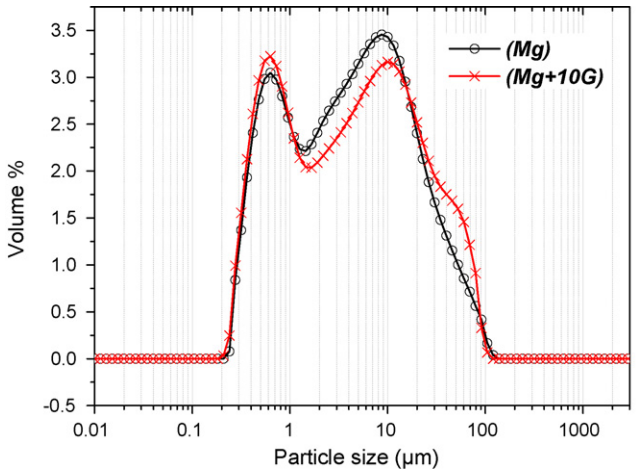

Fig. 14. Particle size distribution of (Mg) after 100 h of milling and (Mg+10G) after 50 h of milling.

ized by the presence of large particles of irregular shape with an average size of 100 μm (Fig. 9b).

As the materials are subjected to reactive mechanical milling, their morphology evolves following a definite sequence that can be organized in three main stages. Both (Mg) and (Mg+10G) follow the same sequence, although in the case of the material with graphite the sequence takes less time. For both materials the first stage occurs during the initial 2 h of milling, and consists in the deformation of the ductile magnesium particles into platelets. In the case of (Mg), the platelets are ~14 μm thick and have a diameter of roughly 350 μm (Fig. 10a). A lateral view of these winding flakes embedded in resin can be appreciated by optical microscopy (Fig. 10b), as well as their tendency to agglomerate by the cold-welding process during milling. In the case of (Mg+10G), the platelets are much smaller, with an approximate diameter of 80 μm and a thickness of ~6 μm (Fig. 10c), and they do not seem to be as cold-welded as the platelets of the material without additive (Fig. 10d). This appears to be a consequence of the lubricant effect of graphite, which at this stage acts as a process control agent during milling. Then, by comparing both materials at this milling stage, we can observe that the anti-sticking effect of graphite renders into a larger unreacted magnesium surface area exposed to hydrogen.

During the second stage, the platelets are welded together and assembled by milling into more or less round and compact particles. Simultaneously with this, the size of the particles is reduced. This stage finishes between 30 and 40 h of milling in the case of (Mg) and is very quick for (Mg+10G), ending approximately after 7 h of milling. This sequence is illustrated in Fig. 11 for (Mg).

Throughout the course of the third stage, some small particles, with sizes below 1 μm, start to appear on the surface of the bigger and compact particles. It seems that these small particles originate from the fragilization of coarser ones, in turn induced by both mechanical milling and hydriding process (Fig. 12).

As milling proceeds, more small particles are produced and aggregate to form agglomerates. In a high magnification SEM image of (Mg+10G) after 50 h of milling (Fig. 13), particles of approximately 100 nm can be found on the surface of an agglomerate. A similar morphology is observed for (Mg) after 100 h milling.

We mentioned before that both materials follow the same sequence during milling, though the sequence takes 100 h for (Mg) and 50 h for (Mg+10G). In microstructural terms, the sequence seems to finish at the same point. We have seen that after milling, the XRD patterns, and particularly the crystallite size, were analogous for (Mg) and (Mg+10G). In Fig. 14 we show that particle size distribution is also alike for (Mg) and (Mg+10G) after milling completion. Additionally, the BET specific surface of both materials is quite similar: 6.32 m^2/g for (Mg) and 7.04 m^2/g for (Mg+10G). Thus, the addition of graphite improves milling, but does not produce a different microstructure, only a shortening of the mechanochemical process.

4. Conclusions

We analyzed the synthesis of magnesium hydride by reactive mechanical milling at room temperature in a low-energy milling device from magnesium powder, and from a mixture of magnesium with 10 wt.% graphite flakes.

The addition of graphite significantly improves the synthesis hydriding rate, halving the time required to achieve full completion of the reaction with hydrogen. During milling, graphite acts as a process control agent which avoids the cold-welding of magnesium particles, and thus favours the particle size refinement, which in turn gives rise to a more efficient hydriding process.

Despite the different times comprised to achieve full hydriding in both materials, 100 h for (Mg) and 50 h for (Mg+10G), their morphology and microstructure evolve following the same sequence. The final materials present very similar morphological and microstructural characteristics.

Analyzing the dehydriding properties of the material without additive by DSC, we found that particle size, instead of crystallite size, seems to be the determining parameter to improve hydrogen desorption from magnesium. As-milled (Mg) with a β-MgH_2 crystallite size of 6 nm, and (Mg) hydride with a crystallite size of 138 nm (obtained after one cycle of dehydriding and re-hydriding the as-milled material in a volumetric device), both with similar particle size distribution, decompose at temperatures that only differ in 15 °C.

When studying the dehydriding properties of (Mg+10G) by DSC, we found that graphite has a catalytic effect on hydrogen desorption that can be appreciated right after 2 h of milling. The two hour-milled material decomposes 100 °C below the temperature decomposition of (Mg) hydride after 2 h of milling, and nearly 60 °C below (Mg) hydride after 100 h of milling. The graphite catalytic effect seems to take place on the surface of magnesium, as suggested by the slight increase of the decomposition temperature with milling time, due to graphite intermixing with magnesium.

Acknowledgements

The authors gratefully acknowledge J.-L. Bobet for making possible the particle size and BET surface measurements. They also acknowledge partial financial support through FONCyT PICT No. 12-12453, PICT No. 821 and PICT No. 20400.

References

[1] A.S. Pedersen, B. Larsen, Int. J. Hydrogen Energy 18 (1993) 297–300.
[2] B. Bogdanovic, T.H. Hartwig, B. Spliethoff, Int. J. Hydrogen Energy 18 (1993) 575–589.
[3] H. Imamura, N. Sakasai, J. Alloys Compd. 231 (1995) 810–814.
[4] J. Huot, E. Akiba, T. Takada, J. Alloys Compd. 231 (1995) 815–819.
[5] K. Gross, P. Spatz, A. Züttel, L. Schlapbach, J. Alloys Compd. 240 (1996) 206–213.
[6] A. Zaluska, L. Zaluski, J.O. Ström-Olsen, J. Alloys Compd. 288 (1999) 217–225.
[7] J. Huot, G. Liang, S. Boily, A. Van Neste, R. Schulz, J. Alloys Compd. 293–295 (1999) 495–500.
[8] F. Gennari, F. Castro, G. Urretavizcaya, J. Alloys Compd. 231 (2001) 46–50.
[9] J. Huot, M.-L. Tremblay, R. Schulz, J. Alloys Compd. 356–357 (2003) 603–607.
[10] R.A. Varin, C. Tomasz, Z.S. Wronski, Nanomaterials for Solid State Hydrogen Storage, Springer, New York, 2009.
[11] J.F.R. de Castro, S.F. Santos, A.L.M. Costa, A.R. Yavari, Botta F.F W.J., T.T. Ishikawa, J. Alloys Compd. 376 (2004) 251–256.
[12] C.X. Shang, M. Bououdina, Y. Song, Z.X. Guo, Int. J. Hydrogen Energy 29 (2004) 73–80.
[13] J.F. Pelletier, J. Huot, M. Sutton, R. Schulz, A.R. Sandy, L.B. Lurio, S.G.J. Mochrie, Phys. Rev. B 63 (2001) 052103–52104.

[14] J. Charbonnier, P. de Rango, D. Fruchart, S. Miraglia, L. Pontonnier, S. Rivoirard, N. Skryabina, P. Vulliet, J. Alloys Compd. 383 (2004) 205–208.
[15] A.R. Yavari, A. LeMoulec, F.R. de Castro, S. Deledda, O. Friedrichs, W.J. Botta, G. Vaughan, T. Klassen, A. Fernandez, Á. Kvick, Scr. Mater. 52 (2005) 719–724.
[16] I.G. Konstanchuk, E.Yu. Ivanov, M. Pezat, B. Darriet, V.V. Boldyrev, P. Hagenmuller, J. Less-Common Met. 131 (1987) 181–189.
[17] Z. Dehouche, T. Klassen, W. Oelerich, J. Goyette, T.K. Bose, R. Schulz, J. Alloys Compd. 347 (2002) 319–323.
[18] J.-L. Bobet, F.J. Castro, B. Chevalier, Scr. Mater. 52 (2005) 33–37.
[19] F.J. Castro, J.-L. Bobet, J. Alloys Compd. 366 (2004) 303–308.
[20] G. Barkhordarian, T. Klassen, R. Bormann, Scr. Mater. 49 (2003) 213–217.
[21] O. Hanada, T. Ichikawa, S. Hino, H. Fujii, J. Alloys Compd. 420 (2006) 46–49.
[22] E. Ivanov, I. Konstanchuk, B. Bokhonov, V. Boldyrev, J. Alloys Compd. 360 (2003) 256–265.
[23] D. Chen, L. Chen, S. Liu, C.X. Ma, D.M. Chen, L.B. Wang, J. Alloys Compd. 372 (2004) 231–237.
[24] M.A. Lillo-Ródenas, Z.X. Guo, K.F. Aguey-Zinsou, D. Cazorla-Amorós, Carbon 46 (2008) 126–137.
[25] Z.G. Huang, Z.P. Guo, A. Calka, D. Wexler, H.K. Liu, Mater. Lett. 61 (2007) 3163–3166.
[26] C.Z. Wu, P. Wang, X. Yao, C. Liu, D.M. Chen, G.Q. Lu, H.M. Cheng, J. Alloys Compd. 414 (2006) 259–264.
[27] Z.G. Huang, Z.P. Guo, A. Calka, D. Wexler, H.K. Liu, J. Alloys Compd. 427 (2007) 94–100.
[28] H. Imamura, N. Sakasai, T. Fujinaga, J. Alloys Compd. 253–254 (1997) 34–37.
[29] H. Imamura, Y. Takesue, T. Akimoto, S. Tabata, J. Alloys Compd. 293–295 (1999) 564–568.
[30] H. Imamura, S. Tabata, Y. Takesue, Y. Sakata, S. Kamazaki, Int. J. Hydrogen Energy 25 (2000) 837–843.
[31] S. Bouaricha, J.-P. Dodelet, D. Guay, J. Huot, R. Schulz, J. Mater. Res. 16 (2001) 2893–2905.
[32] S. Bouaricha, J.P. Dodelet, D. Guay, J. Huot, R. Schulz, J. Alloys. Compd. 325 (2001) 245–251.
[33] H. Imamura, S. Tabata, N. Shigetomi, Y. Takesue, Y. Sakata, J. Alloys Compd. 330–332 (2002) 579–583.
[34] H. Imamura, M. Kusuhara, S. Minami, M. Matsumoto, K. Masanari, Y. Sakata, K. Itoh, T. Fukunaga, Acta Mater. 51 (2003) 6407–6414.
[35] C.X. Shang, Z.X. Guo, J. Power Sources 129 (2004) 73–80.
[36] J.-L. Bobet, E. Grigorova, M. Khrussanova, M. Khristov, P. Stefanov, P. Peshev, D. Radev, J. Alloys Compd. 366 (2004) 298–302.
[37] S. Dal Toè, S. Lo Russo, A. Maddalena, G. Principi, A. Saber, S. Sartori, T. Spataru, Mater. Sci. Eng. B 108 (2004) 24–27.
[38] Z.G. Huang, Z.P. Guo, A. Calka, D. Wexler, J. Wu, P.H.L. Notten, H.K. Liu, Mater. Sci. Eng. A 447 (2007) 180–185.
[39] H. Imamura, I. Kitazawa, Y. Tanabe, Y. Sakata, Int. J. Hydrogen Energy 32 (2007) 2408–2411.
[40] M. Güvendiren, E. Baybörü, T. Öztürk, Int. J. Hydrogen Energy 29 (2004) 491–496.
[41] H.P. Klug, L. Alexander, X-ray Diffraction Procedures for Polycrystalline and Amorphous Materials, Wiley, New York, 1974.
[42] O. Kubaschewski, C.B. Alcock, P.J. Spencer, Materials Thermochemistry, 6th ed. revised, Pergamon Press Ltd., 1993.
[43] R.A. Varin, T. Czujko, Ch. Chiu, Z. Wronski, J. Alloys Compd. 424 (2006) 356–364.
[44] T. Massalski, H. Okamoto, P. Subramanian, L. Kacprzak (Eds.), Binary Alloy Phase Diagrams, ASM, Metals Park, OH, 1990.
[45] H. Nobuko, T. Ichikawa, S.-I. Orimo, H. Fujii, J. Alloys Compd. 366 (2004) 269–273.
[46] O. Friedrichs, F. Aguey-Zinsou, J.R. Ares Fernández, J.C. Sánchez-López, A. Justo, T. Klassen, R. Bormann, A. Fernández, Acta Mater. 54 (2006) 105–110.
[47] K.-F. Aguey-Zinsou, J.R. Ares Fernández, T. Klassen, R. Bormann, Int. J. Hydrogen Energy 32 (2007) 2400–2407.
[48] G. Barkhordarian, T. Klassen, R. Bormann, J. Alloys Compd. 407 (2006) 249–255.